Materials Advances

ROYAL SOCIETY OF CHEMISTRY

PAPER

View Article Online
View Journal | View Issue

Cite this: *Mater. Adv.*, 2026, 7, 2257

Polyaniline-functionalized jute fiber as a sustainable electrode for high-performance supercapacitors

Md. Sanwar Hossain,[a] Md Humayun Kabir,*[b] Md Yeasin Pabel[a] and Sabina Yasmin*[a]

Received 6th October 2025,
Accepted 29th December 2025

DOI: 10.1039/d5ma01144b

rsc.li/materials-advances

A polyaniline (PANI)-modified jute fiber (JF) composite was developed as a low-cost, biodegradable, and high-performance electrode material for supercapacitors. Jute fiber, an abundant natural resource, served as a renewable scaffold for PANI through a simple chemical polymerization process. Composites with varying PANI-to-JF ratios, denoted as PANI/JF-1 to PANI/JF-4, were prepared, among which PANI/JF-3 exhibited the best electrochemical performance. It delivered a high specific capacitance of 3860 ± 204 F g^{-1} at 10 mV s^{-1} (cyclic voltammetry) and 3485 ± 111 F g^{-1} at 5 A g^{-1} (galvanostatic charge–discharge), while retaining 3052 ± 119 F g^{-1} at 50 A g^{-1}, indicating excellent rate capability. The composite achieved a power density of 1692.54 W kg^{-1} at an energy density of 207.72 W h kg^{-1} and maintained 82.27% of its initial capacitance after 3000 charge–discharge cycles at 30 A g^{-1}, demonstrating good cycling stability. FT-IR and density functional theory (DFT) calculations revealed strong interfacial hydrogen bonding between PANI and the cellulose framework, which facilitates charge transfer and increases the effective electrochemically active surface area. These results identify the PANI/JF composite as a scalable bio-based electrode material for high-performance electrochemical energy storage.

1. Introduction

The global transition toward sustainable energy systems has heightened the demand for green, efficient, and renewable energy storage technologies.[1] Electrochemical energy storage devices such as batteries and supercapacitors are increasingly favored as safer, environmentally benign alternatives to fossil fuel-based systems, contributing to economic development and environmental preservation.[2–4] Among these, supercapacitors have emerged as vital components in hybrid energy storage devices, owing to their high power density, rapid charge/discharge rates, and long cycle life.[5] However, conventional electrode materials—including activated carbon, transition metal oxides, and carbon nanotubes—are typically derived from non-renewable sources *via* energy-intensive, hazardous synthesis processes,[6] thereby necessitating scalable, cost-effective, and eco-friendly alternatives that offer competitive or superior electrochemical performance.[7,8]

In this context, biodegradable and natural-based materials are gaining traction as sustainable electrode precursors due to their renewable origin, environmental compatibility, and ability to minimize electronic waste.[9–11] Their light weight, flexibility, and safety also make them ideal for wearable and portable electronics,[12] while aligning with global efforts toward clean energy technologies and circular economies.[13,14] Natural lignocellulosic fibers such as jute (JF), cotton, flax, and hemp are particularly attractive as sustainable scaffolds for supercapacitor electrodes,[15,16] due to their hierarchical fibrous architecture and abundance of functional groups that enable chemical modification or hybridization with electroactive materials.[17,18] Among them, JF stands out for its low cost, biodegradability, high mechanical strength, high aspect ratio, and hydroxyl-rich surface, all of which are favorable for energy storage applications. Nonetheless, pristine natural fibers are intrinsically insulating and lack electrochemical activity.[19,20] To address these limitations, various hybrid strategies have been employed, including surface modification with conductive polymers such as polyaniline (PANI) and polypyrrole (PPy), or conversion into porous carbon through pyrolysis.[21–23] PANI is particularly promising due to its high theoretical capacitance (~1200 F g^{-1}), redox-driven pseudocapacitive behavior, tunable conductivity, and cost-effectiveness.[24] Several studies have validated the potential of bio-derived hybrid systems. For

[a] *Institute of National Analytical Research and Service (INARS), Bangladesh Council of Scientific and Industrial Research (BCSIR), Dhanmondi, Dhaka-1205, Bangladesh. E-mail: sabinayasmin@bcsir.gov.bd*
[b] *Institute of Food Science and Technology (IFST), Bangladesh Council of Scientific and Industrial Research (BCSIR), Dhanmondi, Dhaka-1205, Bangladesh. E-mail: humayunkabir@bcsir.gov.bd*

instance, Tian *et al.* reported a carbonized JF/PANI/rGO composite achieving 229 F g^{-1} with stable cycling,[25] while Zhang *et al.* demonstrated regenerated cellulose fibers from waste flax noil with 510.7 F g^{-1} at 0.5 A g^{-1}.[26] Bonastre *et al.* developed reduced graphene oxide/conducting polymer-coated jute fabrics with 117 F g^{-1} capacitance,[27] and Sajjad *et al.* reported $NiMnO_3$/CNT/PANI ternary hybrid electrodes achieving 1276 F g^{-1} capacitance.[28] Despite this progress, challenges persist. Most lignocellulosic fibers consist primarily of cellulose, hemicellulose, and lignin, all of which are electrically insulating and offer limited surface area and porosity for electrolyte interaction and ion diffusion.[29–32] Consequently, unmodified fibers lack sufficient electroactive sites to support high charge storage. Moreover, achieving uniform PANI coating, maintaining conductivity under high current density, and ensuring long-term cycling stability remain major hurdles.[33] Optimization of synthesis parameters—including the fiber-to-polymer ratio, morphology control, and interfacial engineering—is essential for balancing performance and sustainability.[34]

In this work, we report a simple, scalable method to synthesize PANI-modified jute fiber (PANI/JF) electrodes *via* chemical oxidative polymerization. JF was chosen for its low cost, biodegradability, and compatibility with PANI. By systematically varying JF mass (50–300 mg) at fixed monomer and oxidant concentrations, we optimized the composite formulation. PANI/JF-3 exhibited the highest specific capacitance and superior rate capability, retaining 82.27% of its initial capacitance after 3000 cycles at 50 A g^{-1}. This study addresses three critical needs in sustainable supercapacitor development: high-performance electrodes derived entirely from renewable resources; industrial scalability through simple fabrication, and electrochemical performance comparable to synthetic alternatives. Density functional theory (DFT) calculations further revealed that strong interfacial hydrogen bonding between PANI and cellulose enhances structural integrity and facilitates charge transfer. These findings position PANI/JF composites as promising candidates for truly green and high-performance energy storage systems.

2. Experimental section

2.1 Chemicals and reagents

Aniline (ACS reagent, ≥99.5%, CAS: 62-53-3) and ammonium persulfate (APS, reagent grade, 98%, CAS: 7727-54-0) were purchased from Merck, Germany. Jute fiber (JF) was sourced locally from a farmer in Bangladesh. Hydrochloric acid (37%, CAS: 7647-01-0) and sulfuric acid (95–97%, CAS: 7664-93-9) were obtained from Sigma-Aldrich, Switzerland. Additional reagents including hydrogen peroxide (H_2O_2), sodium silicate (Na_2SiO_3), and sodium carbonate (Na_2CO_3) were also procured from Merck, Germany. All chemicals were of reagent grade and used without further purification. Solutions were prepared using ultrapure deionized (DI) water with a specific conductance below 0.1 μS cm^{-1}.

2.2 Pretreatment of jute fiber

To remove impurities, raw JF was first washed at room temperature and then neutralized in a 0.5 g L^{-1} acetic acid solution for 10 minutes. The material-to-liquor ratio for both neutralization and bleaching was maintained at 1 : 40. The fibers were air-dried using a flat dryer. Bleaching was performed using a solution of H_2O_2 (1.5 g L^{-1}), sodium silicate (3 g L^{-1}), sodium carbonate (3 g L^{-1}), and a wetting agent (1 mL L^{-1}), adjusted to pH 11. The treatment was conducted at 85 °C for 60 minutes in an infrared lab dyeing machine (Xiamen Rapid, China). After bleaching, the fibers were cold-washed and neutralized with 0.5 g L^{-1} acetic acid for 10 minutes at room temperature.

2.3 Synthesis of PANI/JF composites

To synthesize the PANI/JF composite, modified JF was cut into small pieces and used without further modification. The preparation process is illustrated in Scheme 1. A 0.1 M APS

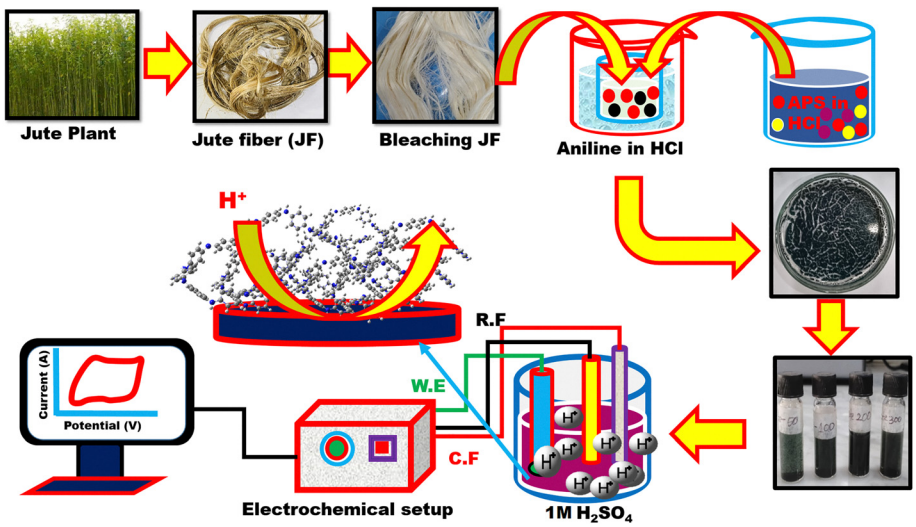

Scheme 1 Schematic illustration of the synthesis of the PANI/JF composite and its application as an electrode material for supercapacitors.

solution (50 mL) and a 0.5 M aniline solution (50 mL) were prepared in 3.0 M HCl. The APS solution was placed in a 250 mL beaker and cooled in an ice bath while stirring at 800 rpm. Once the solution reached 0–5 °C, 200 mg of JF was added, followed by the slow, dropwise addition of the aniline solution. Within five minutes, the solution turned green, indicating the formation of PANI. After completion of the polymerization reaction, the resulting PANI/JF composites were thoroughly washed with deionized water and dried in a vacuum oven at 60 °C. To optimize the JF content for enhanced supercapacitive performance, the same procedure was repeated using 50, 100, and 300 mg of JF, yielding samples denoted as PANI/JF-1, PANI/JF-2, and PANI/JF-4, respectively. The corresponding JF : PANI mass ratios were approximately 1 : 46, 1 : 23, 1 : 12, and 1 : 8.

2.4 Materials characterization

The surface morphology and elemental composition of pristine JF and PANI/JF composites were examined by field-emission scanning electron microscopy (FE-SEM, JEOL JSM-7610F) equipped with energy-dispersive X-ray spectroscopy (EDX), operated at 0.1–30 kV. Transmission electron microscopy (TEM, Talos F200X, Thermo Fisher Scientific) at 200 kV was used for detailed morphological analysis. Fourier-transform infrared (FT-IR) spectra were recorded using a SHIMADZU IR Affinity spectrometer to identify functional groups. X-ray diffraction (XRD) measurements were performed on a Smart Lab SE (Rigaku, Japan) using Cu K_α radiation (λ = 1.541 Å) to investigate the crystalline structure and phase composition.

2.5 Electrochemical measurements

Electrochemical performance was evaluated using a CHI660E electrochemical workstation (CH Instruments, USA) in a standard three-electrode configuration. A glassy carbon electrode (GCE, 3 mm diameter, CHI104) served as the working electrode, a saturated Ag/AgCl/KCl electrode (CHI111) as the reference, and a platinum spiral wire (23 cm, BAS Inc.) as the counter electrode. A 1.0 M H_2SO_4 aqueous solution was used as the electrolyte in all measurements. To prepare the working electrode, 2 mg of the PANI/JF composite was dispersed in 2 mL of DI water and ultrasonicated for 30 minutes. The GCE was polished using 0.05 μm alumina slurry, rinsed thoroughly, and dried at room temperature. Subsequently, 10 μL of the PANI/JF dispersion was drop-cast onto the polished GCE and dried under ambient conditions. The modified electrode was then used for all electrochemical characterizations.

3. Results and discussion

3.1 Characterization

The functional groups of PANI/JF were comprehensively confirmed through FT-IR. FT-IR spectra (Fig. 1a) of pristine JF, pure PANI, and the PANI/JF composite reveal distinct signatures that confirm chemical interactions between PANI and JF. For raw JF, characteristic absorption bands appear at

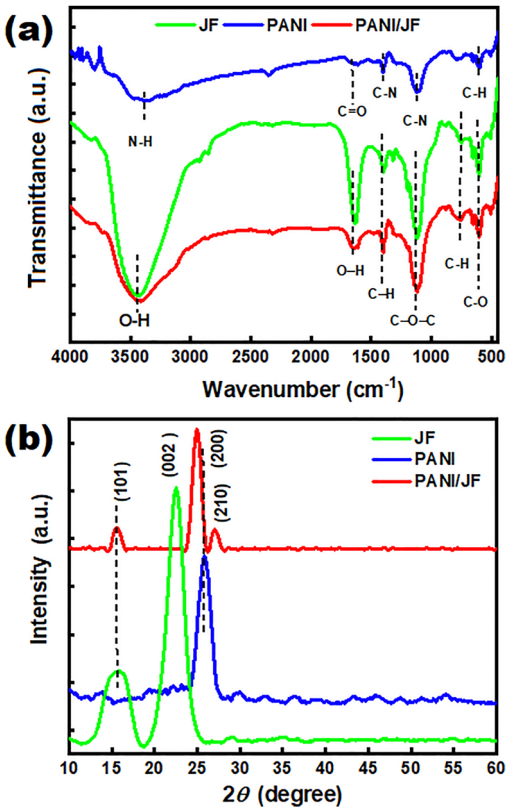

Fig. 1 (a) FT-IR spectra and (b) XRD patterns of JF, PANI, and PANI/JF composites.

3433 cm^{-1} and 1635 cm^{-1}, corresponding to –OH stretching and bending vibrations from cellulose hydroxyl groups and adsorbed water, respectively.[35–37] Additional peaks at 1120 cm^{-1} (C–O–C stretching) and 607 cm^{-1} (C–O bending) arise from glycosidic bonds and lignin content in the fiber structure.[35,38] In the PANI spectrum, prominent peaks at 3397 cm^{-1} (N–H stretching), 1401 cm^{-1} (C–N bending), and 1120 cm^{-1} (C–N stretching) are observed, confirming the presence of amine functionalities and aromatic rings in the PANI backbone.[23,39–41] The PANI/JF composite displays overlapping peaks from both components, but with notable intensity changes: PANI-associated peaks at 1401 cm^{-1} and 1120 cm^{-1} are enhanced, while those from the JF backbone are suppressed—indicating formation of the PANI/JF composite. Furthermore, new bands at 574, 888, and 1171 cm^{-1}, attributed to ring deformation and C–N stretching in PANI, emerge clearly in the composite spectrum, suggesting strong chemical interactions between PANI and cellulose.[38,40,42] The broad N–H band in PANI/JF indicates protonation of PANI. Moreover, the PANI/JF composite shows hydrogen bonding between PANI and jute fiber. In the composite, the O–H stretching peak of jute shifts and broadens, while PANI's N–H stretching broadens and overlaps, indicating interactions between jute's –OH groups and PANI's –NH and –C═N groups. These interactions are further supported by shifts in C–O and C–N stretching. Overall, the hydrogen interaction between jute's hydroxyl groups and PANI's amino or imine groups improves adhesion.

X-ray diffraction patterns (Fig. 1b) further support the structural transformation. Pristine JF exhibits sharp peaks at 16.0° and 22.5°, assigned to the (101) and (002) planes of cellulose I, confirming its semi-crystalline nature.[43] Pure PANI displays a broad diffraction peak at 25.8°, assigned to the (200) plane associated with π–π stacking in the polymer backbone.[44] In the PANI/JF composite, distinct peaks emerge at 16.0°, 24.9°, and 27.1°. Notably, the disappearance of the cellulose (002) peak at 22.5° and the shift of PANI's (200) peak from 25.8° to 24.9° indicate a loss of crystallinity in the cellulose matrix and the formation of strong interfacial hydrogen bonding between PANI and the JF chains.[45,46] The new peak at 27.1°, corresponding to the (210) plane, suggests increased structural ordering in the composite, likely due to improved packing of PANI chains on the fiber scaffold. Collectively, FT-IR and XRD analyses confirm strong molecular interactions between JF and PANI, leading to modified crystallinity and chemical bonding.

Surface morphology, visualized by SEM images (Fig. 2a–f), exhibits a striking transformation upon PANI deposition. Pristine JF (Fig. 2a and b) displays smooth, elongated fibrous structures with rough microgrooves and visible fibrillation—typical of lignocellulosic fibers composed of cellulose, hemicellulose, and lignin.[47] In contrast, the PANI/JF surface (Fig. 2c–f) shows a dramatic evolution into a highly porous architecture with a dense network of tubular and sheet-like nanostructures. The uniformly distributed PANI nanotubes might enhance surface area, providing abundant active sites for charge storage, while the interconnected sheet-like features contribute to improved conductivity. This dual morphology is favorable for facilitating ion transport and electron mobility, both of which are critical for high-performance supercapacitors.[44] TEM images further confirm the nanoscale structure and successful polymer integration (Fig. 2g). The PANI/JF composite reveals a fibrous core with surrounding dark regions of higher electron density, indicative of PANI layers coating the cellulose substrate.[48] The clear contrast between these dark polymer zones and the lighter cellulose matrix confirms uniform polymer deposition and efficient surface coverage, validating the efficacy of the *in situ* polymerization process.

Complementary EDX analysis (Fig. 2h and i) quantifies the elemental composition before and after modification. Pristine JF (Fig. 2h) primarily contains carbon (C) and oxygen (O), with minor amounts of sodium (Na), nitrogen (N), and calcium (Ca) residual elements from biological and chemical pretreatment. After modification, PANI/JF (Fig. 2i) shows a significant increase in carbon content (from 51.57% to 62.77%) due to the carbon-rich PANI chains. More importantly, the nitrogen signal intensifies markedly, confirming PANI incorporation. A relative decrease in oxygen is observed, reflecting the surface-sensitive nature of EDX and the oxygen-free backbone of PANI. EDX confirms elemental integration, particularly the presence

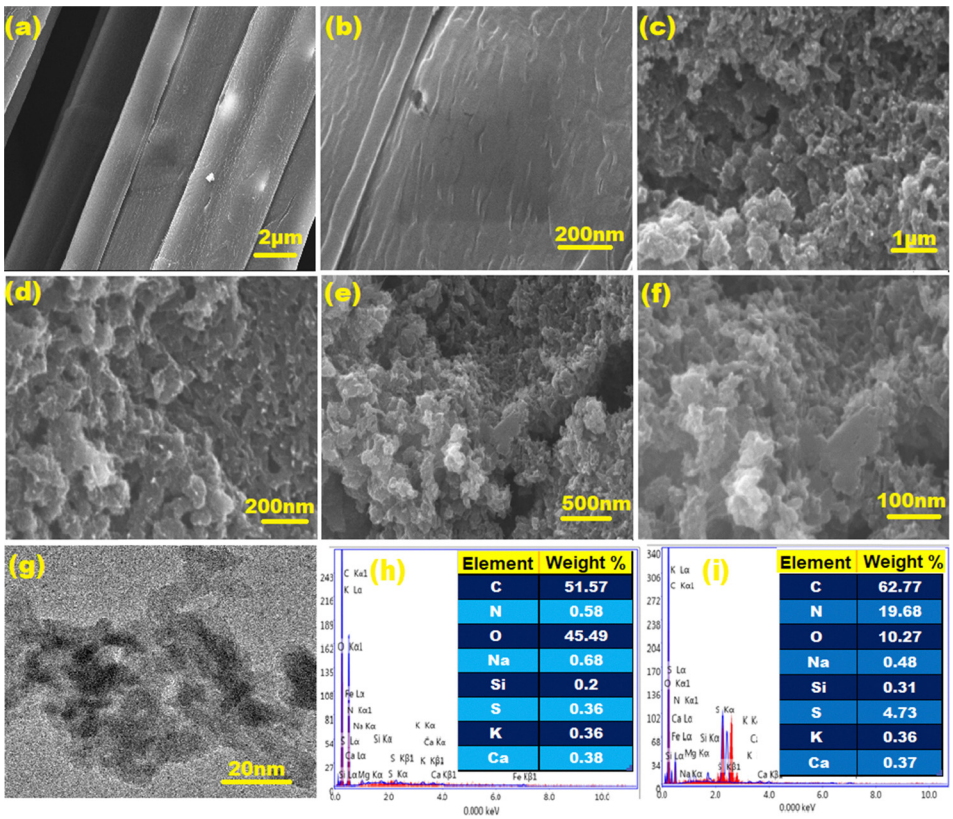

Fig. 2 (a, b) SEM images of raw JF at different magnifications; (c)–(f) SEM images of PANI/JF composites at various magnifications; (g) TEM image of PANI/JF composites; EDX spectra of (h) JF and (i) PANI/JF composites.

of nitrogen from the PANI backbone. Together, these characterizations confirm the successful fabrication of the PANI/JF composite and its structural suitability for electrochemical energy storage.

3.2 Electrochemical performance

The cyclic voltammograms (CVs) of PANI/GC, PANI/JF-1, PANI/JF-2, PANI/JF-3, and PANI/JF-4 electrodes are shown in Fig. 3a. All samples exhibit quasi-rectangular CV profiles with clear redox peaks, indicating a combination of electric double-layer capacitance (EDLC) and pseudocapacitance behavior.[49–51] The appearance of anodic and cathodic peaks suggests surface redox reactions primarily originating from the electroactive PANI component. These redox processes include the reversible transitions between benzoquinone and hydroquinone units, leucoemeraldine and emeraldine forms, and the faradaic transition from emeraldine to pernigraniline.[22,52–54] Such redox transitions are characteristic of the pseudocapacitive behavior of PANI and have been widely reported in the literature. By comparing the integrated area under the CVs, the following trend in electrochemical performance was observed: PANI/JF-3 > PANI/JF-4 > PANI/JF-2 > PANI/JF-1 > PANI/GC. Among these, PANI/JF-3 exhibits the largest CV area, whereas PANI/GC shows the smallest. Notably, the CV curve area of PANI/JF-3 is approximately 11 times greater than that of PANI/GC, indicating a substantially higher charge storage capacity. This enhancement can be directly attributed to the successful incorporation of PANI into the porous JF network, which can improve the electrochemical surface area, electron conductivity, and ion accessibility, properties that were confirmed earlier through SEM (Fig. 2c–f), TEM (Fig. 2g), and FTIR (Fig. 1a) analyses. The porous network formed by the tubular and sheet-like PANI structures on JF facilitates fast ion diffusion and electron transport, contributing to the enhanced performance. To further evaluate the charge storage characteristics, GCD measurements were conducted at a current density of 5 A g^{-1} (Fig. 3b). The discharge time observed from these profiles follows the same trend as CVs: PANI/JF-3 > PANI/JF-4 > PANI/JF-2 > PANI/JF-1 > PANI/GC. This observation is consistent with the morphological and elemental findings (Fig. 2), which showed that PANI/JF-3 had the most uniform and abundant coating of conductive polymer on the fiber surface. A comparison of capacitance values obtained from CV and GCD measurements is presented in Fig. 3c. In all cases, capacitances derived from CV are greater than those from GCD. This is expected, as CV is more sensitive to fast redox processes and pseudocapacitive contributions, which GCD may not fully capture due to limitations in reflecting rapid charge transfer events.[29,55] The consistent dominance of CV-based values suggests that the charge storage in these electrodes is largely pseudocapacitive in nature, especially for PANI-rich compositions like PANI/JF-3.

To understand the scan rate dependence of charge storage, cyclic voltammetry measurements were performed for PANI/JF-3 at scan rates ranging from 10 to 200 mV s^{-1}, as shown in Fig. 4a. With increasing scan rate, both anodic and cathodic peaks shift slightly toward more positive and negative potentials, respectively. This shift is attributed to the increasing internal resistance and kinetic limitations of ion transport at higher scan rates.[56] Despite these shifts, the overall shape and symmetry of the CVs remain intact, suggesting excellent electrochemical stability and reversibility of the redox processes at fast scan rates. This behavior is consistent with the structural robustness and strong interfacial interaction between PANI and JF, as previously revealed through XRD peak shifts and FTIR spectral changes.

Further insight into the charge storage behavior of the PANI/JF composite was obtained by evaluating the variation in specific capacitance with the scan rate, as depicted in Fig. 4b. The specific capacitance (C_{sp}) of PANI/JF-3 was calculated from the CV curves using the following equation:[57]

$$C_{sp} = \frac{\int I \times dV}{\Delta V \times m \times v} \quad (1)$$

where I is the constant discharge current (A), v represents the scan rate, m stands for the mass of the loading material (g), and ΔV is the potential window (V). It is evident that the specific capacitance gradually decreases as the scan rate increases (Fig. 4b). This trend is commonly observed in pseudocapacitive systems and is attributed to the limited time available for faradaic redox reactions and ion adsorption/desorption at higher scan rates.[58] At lower scan rates, ions from the electrolyte have sufficient time to penetrate the porous network and access deeper electroactive sites, thereby contributing to higher

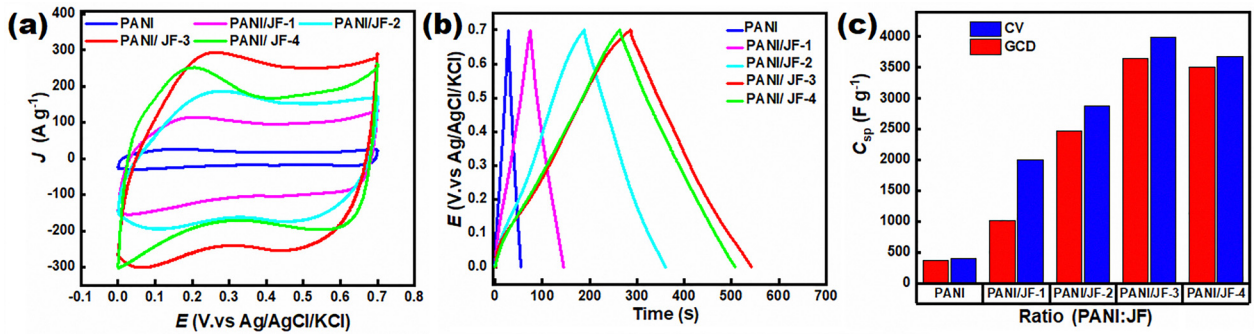

Fig. 3 (a) CVs at a scan rate of 50 mV s^{-1} and (b) GCD profiles at 10 A g^{-1} of PANI and PANI/JF composites in 1.0 M H_2SO_4. (c) Comparison of specific capacitance values calculated from (a) and (b).

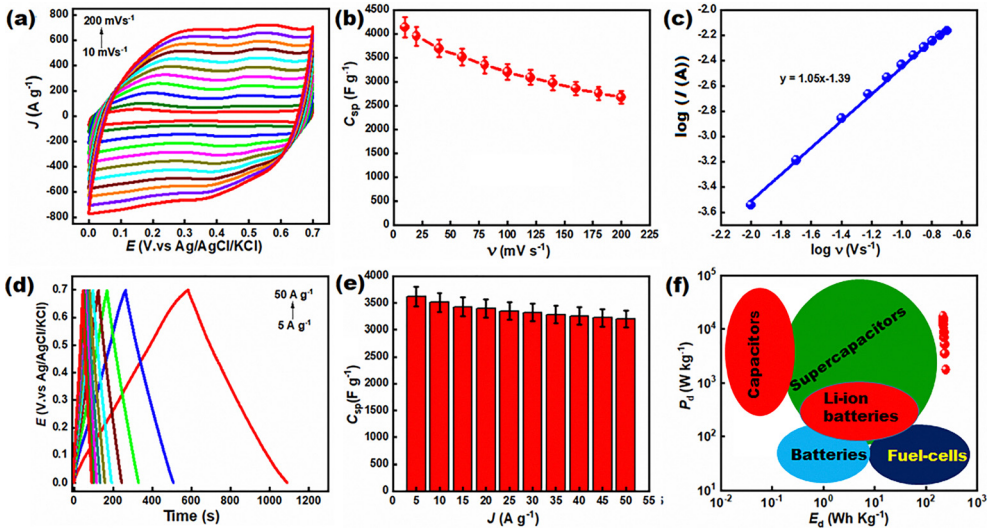

Fig. 4 (a) CVs of PANI/JF composites in 1.0 M H_2SO_4 at varying scan rates; (b) specific capacitance as a function of the scan rate; (c) plot of peak log *I vs.* log *v*. (d) GCD of the PANI/JF composite in 1.0 M H_2SO_4 at different current densities; (e) specific capacitance as a function of current density; (f) Ragone plot comparing the energy–power characteristics of PANI/JF electrodes with representative electrochemical energy storage devices.

charge storage. In contrast, at higher scan rates, only the outer surface of the electrode material is involved in the charge storage process, as ion diffusion into the interior becomes kinetically constrained. This results in a decline in measured capacitance. The situation becomes more pronounced due to the rapid accumulation of electrolyte ions near the electrode/electrolyte interface at higher scan rates, leading to a saturation effect. This electrochemical congestion creates a condition in which there is insufficient time for the ions to undergo diffusion and complete redox interactions at the inner active sites. As a result, a portion of the electroactive surface area remains underutilized during high-speed scans. Despite this, the PANI/JF electrode exhibited outstanding performance across the entire range of scan rates. At a scan rate of 10 mV s^{-1}, the electrode delivered a high specific capacitance of 3860 ± 204 F g^{-1} (mean ± SD, n = 3), showcasing its exceptional charge storage capability. Even when the scan rate was increased to 200 mV s^{-1}, a substantial capacitance of 2306 ± 256 F g^{-1} was retained, indicating that a significant portion of the electroactive sites remained accessible even under fast charging conditions. This remarkable capacitance retention underscores the highly porous and conductive architecture of the PANI/JF composite. The superior electrochemical performance of PANI/JF can be attributed to a combination of key material features: the intrinsic pseudocapacitance of PANI, the hierarchical and porous structure of the jute fiber backbone, and the tunable redox activity of the PANI chains embedded within the JF matrix.[59] These structural and chemical synergies provide extensive electroactive interfaces and facilitate rapid ion and electron transport, even at high scan rates.

To gain a deeper quantitative understanding of the charge storage mechanism and kinetics, we further analyzed the CV curves using the power-law relationship between peak current and the scan rate, as shown in Fig. 4c. The relationship is governed by eqn (2) and (3):[60,61]

$$I = av^b \quad (2)$$

$$\log I = b \log v + \log a \quad (3)$$

where a and b are empirical constants. The b-value is a critical kinetic parameter that signifies the dominant mode of charge storage; a b-value of 1.0 is indicative of surface-controlled capacitive processes—such as EDLC and pseudocapacitance—while a b-value of 0.5 reflects diffusion-controlled processes like faradaic intercalation.[62] Thus, the magnitude of b offers valuable insight into whether charge storage is primarily governed by surface reactions or bulk ion diffusion. In this study, the slope of the log *I vs.* log *v* plot (Fig. 4c) for the cathodic peak of PANI/JF yielded a b-value of 1.05. This slightly super-unity value suggests that the charge storage behavior of the PANI/JF electrode is dominated by capacitive processes, yet not purely surface-confined. The deviation from exactly 1.0 implies the presence of some degree of diffusion-controlled contribution, pointing toward a hybrid electrochemical behavior that involves both faradaic and non-faradaic charge storage mechanisms. Such a combination is advantageous, as it enables the electrode to deliver high power density without significantly compromising energy storage capacity. This finding aligns well with the observed high capacitance, fast redox reversibility, and well-retained performance at high scan rates.

The potential application of the PANI/JF composite as a supercapacitor electrode was further validated through GCD measurements performed over a range of current densities from 5 A g^{-1} to 50 A g^{-1}, as illustrated in Fig. 4d. It is well known that most supercapacitor materials exhibit a significant drop in capacitance when operated at high current densities due to limitations in ion diffusion and charge transfer kinetics.

In contrast, the PANI/JF electrode demonstrated remarkably stable GCD profiles even under high-rate conditions, a result that highlights its robustness and superior electrochemical characteristics. The potential–time curves retained a nearly ideal triangular and symmetric shape at all tested current densities, reflecting a high degree of electrochemical reversibility and efficient charge–discharge behavior. The preservation of this symmetry, particularly at high current densities (up to 50 A g^{-1}), indicates excellent rate capability and minimal resistive losses, underscoring the structural integrity and electrical conductivity of the PANI/JF composite. The specific capacitance (C_{sp}) was calculated from the GCD data using eqn (4):

$$C_{sp} = \frac{I \times t}{m \times \Delta V} \quad (4)$$

where I is the constant discharge current (A), m stands for the mass of the loading material (g), t is the discharging time (s), and ΔV is the potential window (V). At a current density of 5 A g^{-1}, the PANI/JF electrode exhibited a high specific capacitance of 3485 ± 111 F g^{-1}. The high specific capacitance of the PANI/JF electrodes arises from the synergistic effect between PANI and the JF support, which improves electroactive site utilization, ion transport, and redox accessibility of PANI as well as JF. Notably, even at a significantly increased current density of 50 A g^{-1}, C_{sp} remained as high as 3052 ± 119 F g^{-1}, as shown in Fig. 4d. The electrode retains approximately 88% of its initial capacitance over a tenfold increase in current density, demonstrating favorable rate capability for pseudocapacitive charge storage. Such behavior implies that ion transport within the electrode remains efficient even at short timescales, and the redox-active sites remain highly accessible despite the rapid charge–discharge cycling. Furthermore, the near-linear profile of the C_{sp} *versus* current density curve, which remains almost parallel to the *x*-axis, provides additional evidence of the minimal rate-dependent loss in performance. The outstanding rate capability of PANI/JF, demonstrated across a wide range of current densities, positions it as a highly attractive material for high-power supercapacitor applications. Unlike conventional pseudocapacitive electrodes that often suffer from fast capacity fading at high current loads, the PANI/JF system maintains both high energy and power densities with minimal performance degradation. A detailed comparison of the electrochemical performance of PANI/JF with other reported biopolymer-derived supercapacitor electrodes, particularly those activated using H_2SO_4, is provided in Table 1. This comparison further emphasizes the superior capacitance, rate capability, and practical viability of the PANI/JF composite in the context of sustainable, high-performance energy storage systems.

Two critical performance indicators for supercapacitor materials are energy density, E (W h kg^{-1}), and power density, P (W kg^{-1}), as they determine the practical viability of the supercapacitor for real-world applications. For the PANI/JF electrode, these values were calculated based on galvanostatic charge–discharge (GCD) data using eqn (5) and (6):

$$E = \frac{C_{sp} \times \Delta V^2}{2 \times 3600} \quad (5)$$

$$P = \frac{E}{t} \times 3600 \quad (6)$$

where C_{sp} is the specific capacitance (F g^{-1}), ΔV is the potential window (V), and t is the discharge time (s). The Ragone plot was derived from the GCD measurements and is presented in Fig. 4f. At a current density of 5 A g^{-1}, the PANI/JF electrode achieved an impressive power density of 1750 W kg^{-1} and a corresponding energy density of 247.9 W h kg^{-1}. Even at a high current density of 50 A g^{-1}, the system delivered a power density of 16 692.54 W kg^{-1} and an energy density of 207.72 W h kg^{-1}, demonstrating an exceptional ability to maintain energy storage capacity under high power output conditions. The Ragone plot in Fig. 4f illustrates this trend and underscores the excellent rate performance of the PANI/JF electrode. Unlike typical supercapacitor materials, which tend to exhibit a significant trade-off between energy and power densities, the PANI/JF system maintains both high energy and high power outputs, even at extreme current densities. This dual advantage is indicative of the efficient charge transfer kinetics of the composite, high conductivity, and porous nanostructured morphology, which collectively support rapid ion diffusion and stable electron transport pathways. To place the performance of PANI/JF into context, a comparative evaluation was conducted against a variety of existing energy storage technologies, including conventional supercapacitors, lithium-ion batteries, and fuel cells.

Table 1 Comparison of the electrochemical performance of the PANI/JF composite with reported PANI-based electrode materials

Electrode material	Electrolyte	Current density (A g^{-1})	Specific capacitance (F g^{-1})	Ref.
PANI-CB	1 M H_2SO_4	2.0	1486	69
PANI–Co_3O_4	1 M H_2SO_4	1.0	3105.46	70
PANI/PCBM	2 M KOH	2.0	2201	71
LDH@SnO_2@RHC@PAN	3 M KOH	1.0	7684.2	3
PANI–CNTT	1 M H_2SO_4	2.0	1744	72
Polyaniline/Fe_2O_3-decorated graphene	1 M H_2SO_4	2.0	1124	73
$NiMnO_3$/CNT/PANI	1 M H_2SO_4	0.5	1276	28
PANI–Toray	1 M H_2SO_4	1.5	1335	74
PANI/carbon fiber	0.5 M H_2SO_4	0.5	1566	75
Co_3S_4/PANI	1 M H_2SO_4	1.0	1106	76
PANI/JF	1 M H_2SO_4	5.0	3485 ± 111	This study

CB: carbon black; CNT: carbon nanotubes; LDH: layered double hydroxides; PCBM: phenyl-C_{60}-butyric acid methyl ester; RHC: rice husk char.

As shown in Fig. 4f, the PANI/JF electrode outperforms many of these benchmark devices in terms of both energy and power densities. Notably, it surpasses the performance range of traditional supercapacitors, offering significantly higher energy densities while retaining fast charge–discharge capability—a hallmark trait typically associated with supercapacitors. What sets PANI/JF apart is its ability to deliver high power output without compromising energy density, an achievement rarely observed in pseudocapacitive materials. This exceptional characteristic stems from the strong interfacial interaction between PANI and cellulose (as confirmed by DFT in Fig. 6), which ensures efficient electron flow and mechanical stability.

The fundamental electrochemical behavior of the PANI-based supercapacitor was further explored using EIS to gain insights into the charge transfer processes and ion diffusion across the electrode–electrolyte interface, which are critical factors influencing the performance, cycling stability, and rate capability of supercapacitors.[63,64] These transport properties were evaluated for both PANI/GC and PANI/JF electrodes to determine the effect of incorporating PANI into the natural fiber substrate.[65] The Nyquist plots, presented in Fig. 5a, were recorded over a frequency range of 0.1 Hz to 100 kHz with a perturbation amplitude of 5 mV. The spectra reveal a semicircular arc in the high-frequency region, indicative of charge transfer resistance (R_{ct}), and a linear segment in the low-frequency region, associated with ion diffusion behavior. Notably, the PANI/JF electrode shows a smaller semicircle diameter and a steeper linear slope compared to PANI/GC, implying significantly improved charge transfer kinetics and more efficient ion diffusion pathways. These enhancements reflect the influence of the porous and conductive nature of the PANI-modified jute matrix. Further analysis using an equivalent circuit model, shown as an inset in Fig. 5a, supports these findings. The model includes components for equivalent series resistance (R_s), R_{ct}, Warburg impedance (W), double-layer capacitance (C_{dl}), and pseudocapacitive capacitance (C_p). The R_s value, determined from the intercept of the Nyquist curve with the real axis, represents the internal resistance of the electrode system. A comparison reveals that the PANI/JF electrode has a lower R_s (6.84 Ω) than PANI/GC (7.22 Ω), indicating reduced internal resistance and enhanced electrical conductivity due to the PANI incorporation. The diameter of the semicircle reflects the R_{ct}, which is also markedly lower for PANI/JF (0.36 Ω), indicating faster electron transfer kinetics. This improvement aligns with the strong hydrogen bonding and interfacial compatibility between PANI and cellulose observed in the DFT analysis (Fig. 6) and supports the superior electrochemical performance observed in CV and GCD studies. Additionally, the value of W, which quantifies ion diffusion resistance, is found to be 2.64 Ω for PANI/JF, suggesting that the porous fiber framework facilitates efficient ion transport by providing well-connected diffusion pathways. Capacitive contributions were also analyzed from the circuit model. The PANI/JF electrode shows two capacitance components: C_{dl} (1.4 μF), representing the EDLC at the electrode–electrolyte interface, and C_p (442 mF), representing the pseudocapacitance arising from reversible faradaic redox reactions. These faradaic processes involve charge transfer reactions such as redox transitions, ion adsorption/desorption, or surface intercalation, which substantially increase the total capacitance and energy storage capacity of the system. The high value of C_p, in particular, underscores the dominant contribution of pseudocapacitive mechanisms to the overall charge storage in the PANI/JF system. Therefore, the presence of low R_s, minimal R_{ct}, low W, and substantial C_p confirms that the PANI/JF composite possesses superior conductivity, fast electron/ion transport kinetics, and high

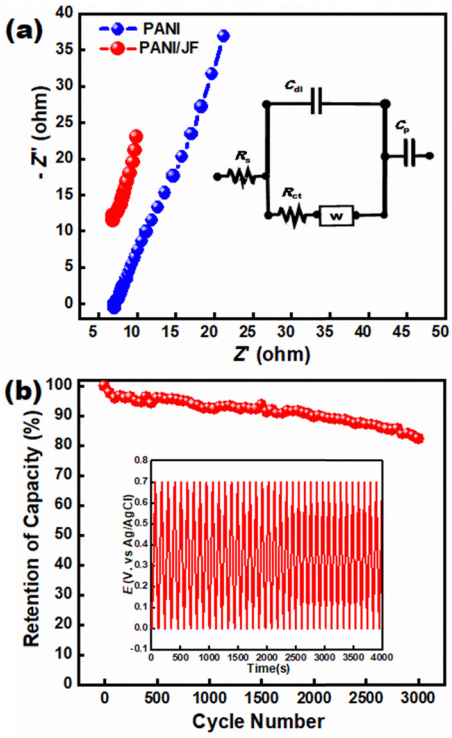

Fig. 5 (a) Nyquist plots of the PANI/JF composite and PANI film electrodes recorded in 1.0 M H_2SO_4; the inset shows the corresponding equivalent circuit. (b) Cycling stability of the PANI/JF composite over 3000 charge–discharge cycles at 30 A g^{-1} in 1.0 M H_2SO_4.

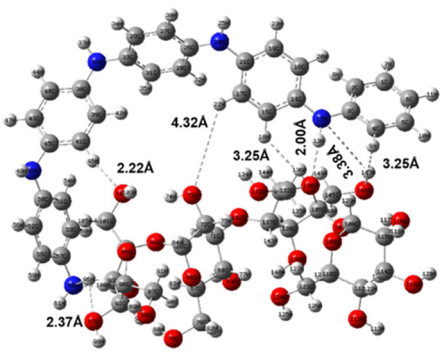

Fig. 6 Optimized structure of the PANI–cellulose (JF) complex calculated by the B3LYP/6-311 level of theory. Carbon (C), oxygen (O), nitrogen (N), and hydrogen (H) atoms are represented by gray, red, blue, and white spheres, respectively.

capacitive efficiency. These findings validate the effectiveness of integrating conductive PANI into a biomass-derived fiber matrix and further support the role of rational interfacial design in producing high-performance, scalable electrodes for next-generation supercapacitor applications.

Furthermore, the cycling stability of the electrode material is a critical parameter in determining its long-term suitability for energy storage applications. To assess this, the GCD measurements were carried out at a high current density of 30 A g^{-1} over 3000 continuous cycles. As shown in Fig. 5b, the PANI/JF electrode exhibited excellent cycling durability, retaining 82.27% of its initial capacitance after 3000 cycles. The capacitance retention was calculated by taking the ratio of the final specific capacitance (after 3000 cycles) to the initial specific capacitance obtained from the GCD curves. This retention performance is indicative of the robust electrochemical reversibility and structural stability of the composite under prolonged high-rate charge–discharge conditions. To ensure the reliability and consistency of these results, the experiment was repeated multiple times under identical conditions, and the reproducibility of the data was confirmed. The minimal degradation observed over extended cycling highlights the mechanical integrity of the jute fiber scaffold and the electrochemical stability of the polyaniline coating, further establishing PANI/JF as a promising and durable electrode material for high-performance supercapacitors.

3.3 Interfacial interaction between PANI and JF

The remarkably high specific capacitance observed for the PANI/JF-based supercapacitor can be attributed, in large part, to the strong interfacial interactions between PANI and cellulose. These interactions were investigated through density functional theory (DFT) calculations, which provide molecular-level insights into the binding and compatibility between the two components.[66–68] The optimized structure of the PANI–cellulose complex was obtained at the B3LYP/6-311 level of theory, and the results are presented in Fig. 6 and Table S3 (See SI for details). The optimized structure clearly reveals the formation of an extensive hydrogen bonding network between the hydroxyl-rich cellulose surface and the functional groups of PANI. Several significant interfacial interactions are identified between oxygen atoms from cellulose and hydrogen atoms from PANI, with hydrogen bond distances as follows: 2.22 Å (O102···H46), 2.94 Å and 2.00 Å (O138···H18), 2.31 Å (O97···H96), 4.37 Å (O73···H22), and 3.25 Å (O146···H9), as listed in Table S5 and shown in Fig. 6. In addition to oxygen-centered hydrogen bonds, nitrogen atoms in the PANI backbone were found to participate in hydrogen bonding with cellulose-bound hydrogens, with the following bond distances: 2.91 Å (N60···H96), 2.13 Å (N60···H95), 3.38 Å (N12···H1447), and 3.26 Å (N12···H149). These interactions, illustrated by dashed lines in the DFT model, underscore the strong binding affinity and interfacial compatibility between PANI and cellulose. The calculated interaction energy of −51.722 kJ mol^{-1} (Table S4) confirms that the formation of the PANI–cellulose complex is thermodynamically favorable and structurally stable. These interfacial hydrogen bonds are not merely structural—they also play a critical role in electrochemical performance enhancement. The intimate contact facilitated by hydrogen bonding ensures uniform PANI distribution over the cellulose matrix and enables efficient electron transport across the composite interface. This molecular-level adhesion supports the morphological observations from SEM and TEM, where a uniform, porous coating of PANI was evident on the JF surface. Furthermore, the fibrous and porous nature of cellulose inherently improves electrolyte accessibility and ion diffusion, leading to greater exposure of redox-active sites and enhanced faradaic contributions during charge/discharge cycles. Together, the hydrogen bonding network and the morphological compatibility between PANI and cellulose explain the exceptionally high specific capacitance observed for PANI/JF and its stable performance even at high scan rates. These theoretical insights affirm that interfacial chemistry is a determining factor in the design of efficient, bio-derived energy storage materials. Additionally, numerous intermolecular bonds were observed between the cellulose and PANI chains, contributing to the stability and performance of the composite, as detailed in Tables S3–S5. The nature and number of these bonds, especially the coexistence of both oxygen–hydrogen and nitrogen–hydrogen interactions, were thoroughly analyzed and emphasized in this study.

4. Conclusions

We have successfully developed a high-performance supercapacitor electrode by integrating polyaniline (PANI) with jute fiber (JF), a naturally abundant and renewable biomass. Synthesized through a facile one-step chemical polymerization method, the resulting PANI/JF composite demonstrates strong electrochemical performance. The electrode delivers a high specific capacitance of 3485 ± 111 F g^{-1} at 5 A g^{-1} and achieves an energy density of 207.72 W h kg^{-1} at a power density of 1692.54 W kg^{-1} under electrochemical testing conditions. Moreover, the composite exhibits good cycling stability, retaining 82.27% of its initial capacitance after 3000 charge–discharge cycles at 30 A g^{-1}, while maintaining high capacitance at current densities up to 50 A g^{-1}. The enhanced performance arises from the synergistic interplay between the porous fibrous structure of JF, which facilitates efficient ion transport and electrolyte accessibility, and the high electrical conductivity and redox activity of PANI, enabling the coexistence of electric double-layer and pseudocapacitive charge-storage mechanisms. Density functional theory calculations reveal the presence of strong interfacial hydrogen bonding between PANI and the cellulose framework, which enhances charge transfer and structural integrity, providing a molecular-level rationale for the observed electrochemical stability and performance. Overall, this study demonstrates that biomass-derived fibrous scaffolds combined with conducting polymers represent a viable and scalable strategy for the development of advanced supercapacitor electrodes.

Author contributions

Md. Sanwar Hossain: experimental execution, data analysis, writing – original draft; Md Humayun Kabir: conceptualization, methodology, project administration, writing – review & editing, supervision; Md Yeasin Pabel: data analysis, methodology, writing – review & editing. Sabina Yasmin: conceptualization, methodology, writing – review & editing, supervision.

Conflicts of interest

The authors declare no conflicts of interest.

Data availability

Data will be available upon request.

Supplementary information (SI) is available. See DOI: https://doi.org/10.1039/d5ma01144b.

Acknowledgements

The authors are grateful to the Bangladesh Council of Scientific and Industrial Research (BCSIR) for financial support (R&D ref. no. 39.02.0000.011.14.180.2024/1116, date: 14.01.2025) and facilities.

References

1 P. J. Megía, A. J. Vizcaíno, J. A. Calles and A. Carrero, *Energy Fuels*, 2021, **35**, 16403–16415.
2 J. Ding, Y. Yang, J. Poisson, Y. He, H. Zhang, Y. Zhang, Y. Bao, S. Chen, Y. M. Chen and K. Zhang, *ACS Energy Lett.*, 2024, **9**, 1803–1825.
3 A. Kiani, E. Ahmadi and Z. Mohamadnia, *ACS Appl. Energy Mater.*, 2024, **7**(21), 9892–9901, DOI: 10.1021/acsaem.4c01933.
4 W. Zhao, S. J. B. Rubio, Y. Dang and S. L. Suib, *ACS ES&T Eng*, 2022, **2**, 20–42.
5 M. Ayaz, S. S. Shah, M. Younas, U. Safder, I. Khan, M. A. Aziz, Adnan, M. Oyama, J. H. Rice, M. N. Tahir and M. Ashraf, *J. Energy Storage*, 2025, **110**, 115291.
6 A. M. Afridi, M. Aktary, S. Shaheen Shah, S. I. Mitu Sheikh, G. Jahirul Islam, M. Nasiruzzaman Shaikh and M. Abdul Aziz, *Chem. Rec.*, 2024, **24**, e202400144.
7 S. Dühnen, J. Betz, M. Kolek, R. Schmuch, M. Winter and T. Placke, *Small Methods*, 2020, **4**, 2000039.
8 Y. Pabel, H. Kabir, S. Hossain and S. Yasmin, *Mater. Adv.*, 2025, **6**, 2243–2252.
9 N. Choudhary, S. Singh, S. Bhardwaj, S. Gupta, U. Nandi, R. Chandra and P. K. Maji, *Carbohydr. Polym. Technol. Appl.*, 2024, **7**, 100416.
10 S. Dey, G. T. N. Veerendra, S. S. A. B. Padavala and A. V. P. Manoj, *Green Anal. Chem.*, 2023, **7**, 100085.
11 X. Chen, M. Kurdve, B. Johansson and M. Despeisse, *Sustain. Prod. Consum.*, 2023, **38**, 13–27.
12 M. Pantrangi, E. Ashalley, M. K. Hadi, H. Xiao, Y. Zhang, W. Ahmed, N. Singh, A. Alam, U. Younis, F. Ran, P. Liang and Z. Wang, *Energy Storage Mater.*, 2024, **73**, 103791.
13 J. J. Klemeš, A. Foley, F. You, K. Aviso, R. Su and A. Bokhari, *Renewable Sustainable Energy Rev.*, 2023, **177**, 113143.
14 M. Islam, S. Hossain, N. Padmanathan and K. M. Razeeb, *Mater. Adv.*, 2025, **6**, 7895–7905, DOI: 10.1039/d5ma00830a.
15 M. S. Hossen, T. Islam, S. M. Hoque, A. Islam, M. M. Bashar and G. Bhat, *ACS Omega*, 2024, **9**, 35384–35393.
16 M. Dulal, S. Afroj, J. Ahn, Y. Cho, C. Carr, I.-D. Kim and N. Karim, *ACS Nano*, 2022, **16**, 19755–19788.
17 A. C. Bressi, A. Dallinger, Y. Steksova and F. Greco, *ACS Appl. Mater. Interfaces*, 2023, **15**, 35788–35814.
18 C. Hu, P. Liu, Z. Song, Y. Lv, H. Duan, L. Xie, L. Miao, M. Liu and L. Gan, *Chin. Chem. Lett.*, 2025, **36**, 110381.
19 N. Sharma, K. Mishra, N. Singh, S. S. Siwal, P. Hart and V. K. Thakur, *Macromol. Mater. Eng.*, 2025, **310**, 2400129.
20 S. Jha, Y. Qin, Y. Chen, Z. Song, L. Miao, Y. Lv, L. Gan and M. Liu, *ACS Sustainable Chem. Eng.*, 2025, **13**(50), 21787–21800, DOI: 10.1021/acssuschemeng.5c10802.
21 T. Islam, M. H. Chaion, M. A. Jalil, A. S. Rafi, F. Mushtari, A. K. Dhar and S. Hossain, *SPE Polym.*, 2024, **5**, 481–506.
22 M. S. Hossain, M. H. Kabir, M. A. A. Shaikh, M. Y. Pabel and S. Yasmin, *Mater. Chem. Phys.*, 2024, **322**, 129586.
23 M. S. Hossain, N. Padmanathan, M. M. R. Badal, K. M. Razeeb and M. Jamal, *ACS Omega*, 2024, **9**, 40122–40133.
24 M. H. Gharahcheshmeh and K. Chowdhury, *Energy Adv.*, 2024, **3**, 2668–2703, DOI: 10.1039/d4ya00504j.
25 Y. Tian, J. Ouyang, L. Wang, Y. Wang, M. Cheng, W. Yin, X. Ren, Z. Liu, J. Luo and Y. Luo, *J. Energy Storage*, 2025, **120**, 116500.
26 Q. Zhang, R. Wang, Y. Zou, J. Mao and L. Wang, *Ind. Crops Prod.*, 2022, **176**, 114377.
27 J. Bonastre, J. Molina and F. Cases, *J. Energy Storage*, 2023, **69**, 107936.
28 L. Sajjad, G. Ali, M. A. Mansoor and M. F. Khan, *J. Energy Storage*, 2023, **72**, 108351.
29 N. P. D. Ngidi, A. F. Koekemoer and S. S. Ndlela, *J. Energy Storage*, 2024, **89**, 111638.
30 M. M. Islam, *Sustainable Energy Fuels*, 2024, **8**, 1823–1871.
31 E. R. Ezeigwe, R. N. Dunne, S. B. B. Solberg, J. J. Lamb, J. Wind and O. S. Burheim, *J. Energy Storage*, 2025, **109**, 115253.
32 J. Zhang, W. Wang, S. Hao, H. Zhu, C. Wang, Z. Hu, Y. Yu, F. Wang, P. Fu, C. Shao, J. Yang and H. Cong, *Nano-Micro Lett.*, 2025, **18**, 34.
33 H. Wang, J. Lin and Z. X. Shen, *J. Sci. Adv. Mater. Devices*, 2016, **1**, 225–255.
34 X. Li, X. Chen, Z. Jin, P. Li and D. Xiao, *Mater. Chem. Front.*, 2021, **5**, 1140–1163.
35 H. Wang, H. Memon, E. A. M. Hassan and S. Miah, *Materials*, 2019, **12**(8), 1226, DOI: 10.3390/ma12081226.
36 S. Yasmin, M. G. Azam, M. S. Hossain, U. S. Akhtar and M. H. Kabir, *Heliyon*, 2024, **10**, e33317.
37 H. Kabir, J. Miah, A. K. Mohiuddin, S. Hossain, B. P. Upoma, A. A. Shaikh, Y. Pabel, F. Mojumder, R. Mahmud,

N. I. Tanvir and S. Yasmin, *ACS Sustainable Resour. Manage.*, 2025, **2**(2), 256–266, DOI: 10.1021/acssusresmgt.4c00296.
38 B. P. Upoma, S. Yasmin, A. A. Shaikh, T. Jahan, A. Haque, M. Moniruzzaman and H. Kabir, *ACS Omega*, 2022, **7**(34), 29655–29665, DOI: 10.1021/acsomega.2c01919.
39 S. Yasmin, M. S. Ahmed and S. Jeon, *J. Electrochem. Soc.*, 2015, **162**, B363, DOI: 10.1149/2.0751514jes.
40 M. S. Hossain, M. H. Kabir, M. A. Ali Shaikh, M. A. Haque and S. Yasmin, *RSC Adv.*, 2024, **14**, 1431–1444.
41 A. Perumal, R. Kanumuri, S. K. Rayala, R. Nallaiyan, X. Kong, C. Zeng, X. Wang, J. Huang, C. Li, J. Fei, J. Li, Q. Feng, S. Yasmin, D. Park, S. Jeon, N. Roy, M. Kabir and S. Jeon, *J. Electrochem. Soc.*, 2016, **9**, B491–B498.
42 F. Mojumder, S. Yasmin, M. A. A. Shaikh, P. Chowdhury and M. H. Kabir, *J. Hazard Mater. Adv.*, 2024, 100429.
43 N. A. V. Santos, M. T. R. Pulido, D. von, C. Tumacder and K. L. M. Taaca, *Carbohydr. Polym. Technol. Appl.*, 2021, **2**, 100129.
44 T. V. Jinitha, K. P. Safna Hussan, N. Subair, V. Shaniba, A. K. Balan and E. Purushothaman, *RSC Adv.*, 2018, **8**, 34388–34396.
45 S. Singla and A. Dhinojwala, *ACS Nano*, 2017, **11**(5), 4899–4906.
46 A. Etale, A. J. Onyianta, S. R. Turner and S. J. Eichhorn, *Chem. Rev.*, 2023, **123**, 2016–2048.
47 P. Swain, R. Pal, D. Chouhan and S. P. Mohanty, *J. Nat. Fibers*, 2022, **19**, 14924–14934.
48 G. V. Hartland, L. V. Besteiro, P. Johns and A. O. Govorov, *ACS Energy Lett.*, 2017, **2**, 1641–1653.
49 X. You, M. Misra, S. Gregori and A. K. Mohanty, *ACS Sustainable Chem. Eng.*, 2018, **6**, 318–324.
50 M. S. Chaudhary, D. Seth, Waris, S. Hasan, S. Sultana, M. A. Haider, M. Agarwal and M. Z. Khan, *ACS Appl. Energy Mater.*, 2025, **8**, 245–258.
51 N. Naresh, Y. Zhu, Y. Fan, J. Luo, T. Wang, I. P. Parkin and B. D. Boruah, *Nano Lett.*, 2024, **24**, 11059–11066.
52 A. Andriianova, Y. Biglova and A. Mustafin, *RSC Adv.*, 2020, **10**, 7468–7491.
53 Y. Yeszhan, S. Duisenbekov, D. Kurmangaliyeva, D. Kazhigitova, P. Askar, Y. Tileuberdi, A. Konarov, S. Adilov and N. Nuraje, *RSC Adv.*, 2025, **15**, 1205–1211.
54 Z. Li, S. Bai, K. Chen, Y. Liu, Y. Zhang and S. Liu, *Chem. Eng. J.*, 2024, **481**, 148486.
55 C. Zhang, S. Bhoyate, C. Zhao, P. Kahol, N. Kostoglou, C. Mitterer, S. Hinder, M. Baker, G. Constantinides, K. Polychronopoulou, C. Rebholz and R. Gupta, *Catalysts*, 2019, **9**, 176.
56 W. Niu and Y. Yang, *ACS Energy Lett.*, 2018, **3**, 2796–2815.
57 Y. Lan and L. Changshi, *J. Energy Storage*, 2024, **75**, 109688.
58 S. Sharma and P. Chand, *Results Chem*, 2023, **5**, 100885.
59 A. T. S. C. Brandão, S. State, R. Costa, P. Potorac, J. A. Vázquez, J. Valcarcel, A. F. Silva, L. Anicai, M. Enachescu and C. M. Pereira, *ACS Omega*, 2023, **8**, 18782–18798.
60 M. A. Hasan and M. M. Islam, *J. Energy Storage*, 2024, **98**, 113015.
61 Y. Jiang, Z. Sun, C. Tang, Y. Zhou, L. Zeng and L. Huang, *Appl. Catal., B*, 2019, **240**, 30–38.
62 P. Tiwari, J. Jaiswal and R. Chandra, *Electrochim. Acta*, 2019, **324**, 134767.
63 A. C. Lazanas and M. I. Prodromidis, *ACS Meas. Sci. Au*, 2023, **3**, 162–193.
64 L. A. Santa-Cruz, F. C. Tavares, L. F. Loguercio, C. I. L. dos Santos, R. A. Galvão, O. A. L. Alves, M. Z. Oliveira, R. M. Torresi and G. Machado, *Phys. Chem. Chem. Phys.*, 2024, **26**, 25748–25761.
65 R. Bogdanowicz, A. Dettlaff, F. Skiba, K. Trzcinski, M. Szkoda, M. Sobaszek, M. Ficek, B. Dec, L. Macewicz, K. Wyrębski, G. Pasciak, D. Geng, A. Ignaczak and J. Ryl, *J. Phys. Chem. C*, 2020, **124**, 15698–15712.
66 M. Bursch, J. M. Mewes, A. Hansen and S. Grimme, *Angew. Chem., Int. Ed.*, 2022, **61**, e202205735.
67 H. P. Beck, M. Zhou, P. Hasanovic, E. Gießelmann and M. Springborg, *J. Chem. Educ.*, 2021, **98**, 3207.
68 M. S. Hossain, S. Yasmin and M. H. Kabir, *J. Saudi Chem. Soc.*, 2024, **28**, 101873.
69 M. A. Bavio, G. G. Acosta and T. Kessler, *Int. J. Hydrogen Energy*, 2014, **39**, 8582–8589.
70 Y. Fan, H. Chen, Y. Li, D. Cui, Z. Fan and C. Xue, *Ceram. Int.*, 2021, **47**, 8433–8440.
71 A. Kiani, E. Ahmadi and Z. Mohamadnia, *ACS Appl. Energy Mater.*, 2024, **7**, 9892–9901.
72 M. A. Bavio, G. G. Acosta and T. Kessler, *J. Power Sources*, 2014, **245**, 475–481.
73 A. Gupta, S. Sardana, J. Dalal, S. Lather, A. S. Maan, R. Tripathi, R. Punia, K. Singh and A. Ohlan, *ACS Appl. Energy Mater.*, 2020, **3**, 6434–6446.
74 R. Soni, V. Kashyap, D. Nagaraju and S. Kurungot, *ACS Appl. Mater. Interfaces*, 2018, **10**, 676–686.
75 J. Du, Y. Li, Q. Zhong, J. Yang, J. Xiao, D. Chen, F. Wang, Y. Luo, K. Chen and W. Li, *ACS Omega*, 2020, **5**, 22119–22130.
76 M. Xu, H. Guo, T. Zhang, J. Zhang, X. Wang and W. Yang, *J. Energy Storage*, 2021, **35**, 102303.